Selective Detection in Impulsive Low-Frequency Raman Imaging Using Shaped Probe Pulses

Siddarth Shivkumar,[1] Dekel Ranann,[2] Samuel Metais,[1] Sisira Suresh,[1] Nicolas Forget,[3] Randy Bartels,[4] Dan Oron,[2] and Hervé Rigneault[1,*]

[1] *Aix Marseille Université, CNRS, Centrale Marseille, Institut Fresnel, Marseille, France*
[2] *Department of Physics of Complex Systems, The Weizmann Institute of Science, Rehovot 76100, Israel*
[3] *Fastlite, Antibes 06600, France*
[4] *Departments of Electrical and Computer Engineering and Biomedical Engineering, Colorado State University, Fort Collins, USA*

(Received 8 September 2022; revised 21 October 2022; accepted 1 May 2023; published 23 May 2023)

Impulsive stimulated Raman scattering (ISRS) using a single short femtosecond pump pulse to excite molecular vibrations offers an elegant pump-probe approach to perform vibrational imaging below 200 cm^{-1}. One shortcoming of ISRS is its inability to offer vibrational selectivity as all the vibrational bonds whose frequencies lie within the short pump-pulse bandwidth are excited. To date, several coherent control techniques have been explored to address this issue and selectively excite a specific molecular vibration by shaping the pump pulse. There has not been any systematic work that reports an analogous shaping of the probe pulse to implement preferential detection. In this work, we focus on vibrational imaging and report vibrational selective detection by shaping the probe pulse in time. We demonstrate numerically and experimentally two pulse-shaping strategies with one functioning as a vibrational notch filter and the other functioning as a vibrational low-pass filter. This enables fast (25 μs/pixel) and selective hyperspectral imaging in the low-frequency regime (<200 cm^{-1}).

DOI: 10.1103/PhysRevApplied.19.054075

Optical microscopy has evolved as an indispensable tool in bioimaging owing to the abundance of chemical-specific information that can be accessed. Fluorescence microscopy has demonstrated sensitivity up to the single molecule level, however, it is limited by the necessity of fluorescence tags or biomarkers [1]. Vibrational imaging, on the other hand, sacrifices sensitivity but offers the possibility to perform label-free imaging. Further, vibrational imaging offers a simple and elegant way to access intramolecular chemical-specific information (frequencies >200 cm^{-1}) and intermolecular structure-specific information (frequencies <200 cm^{-1}) [2–5]. In particular, Raman microspectroscopy has become a routine tool used for material characterization owing to the availability of a range of microscope objectives in the visible and the near-infrared ranges [6]. Despite all the advantages that Raman microspectroscopy brings to the table, the weak Raman scattering cross section results in increased integration times, thereby impacting the imaging speed. This low-signal problem is circumvented in coherent Raman scattering (CRS) where the rate of Raman scattering is increased by orders of magnitude [7–10]. In CRS, the molecules are coherently driven into vibration by using two light fields (namely pump and Stokes) whose beat frequency matches the frequency of the molecular vibration. Enabled by CRS, video-rate imaging and near-video rate hyperspectral imaging has been achieved in the high-frequency regime (frequencies >200 cm^{-1}) [11–13].

The enhanced speed of imaging that is achieved in the high-frequency regime by CRS has not found an immediate extension in low-frequency regime (frequencies <200 cm^{-1}). The limitation to fast imaging in this case comes from the fact that the CRS modalities use chromatic filters to isolate the Raman signal from the input fields. Given that even the best optical edge filters in the market today have a finite transition slope, it thereby results in longer integration times to detect lower-frequency shifts.

Impulsive stimulated Raman scattering (ISRS) [14,15] overcomes the bottleneck faced by CRS in the low-frequency regime by taking a time-domain approach. In ISRS, demonstrated by Silvestri *et al.* [16], both the pump and the Stokes fields required to excite a Raman-active mode are obtained from the bandwidth of a single femtosecond pulse. In the time domain, this means that all modes whose vibrational periods are longer than the pump-pulse duration get excited and prepare a vibrational coherence in the focal volume. This vibrational coherence then leads to a time-varying perturbation of the

*herve.rigneault@fresnel.fr

effective linear optical susceptibility, which can be linked to a transient refractive index [17]. A probe pulse arriving at different pump-probe delays senses this transient refractive index and undergoes diffraction [2,16,18], modulation in its spatial profile with propagation [19], a shift in its spectral centroid [20–27], change in its state of polarization [28–30], and accumulates a phase shift [23,31–34]. By looking at one of these read-out mechanisms through a dedicated experimental configuration, the temporal Raman response can be retrieved—a simple Fourier transform of which or model estimation like linear predictive singular value decomposition (LPSVD) [31] gives access to the molecular spectrum.

With most of the work done until the late 1990s dedicated to spectroscopic applications [18,20–22], an imaging application of ISRS was demonstrated by Koehl *et al.* [35], who imaged polariton propagation in a ferroelectric crystal. Following this, with the advent of fast delay scanning techniques, Domingue *et al.* used a spinning window pump-probe delay scanner to acquire hyperspectral images of $Bi_4Ge_3O_{12}$ and $CdWO_4$ crystals at pixel dwell times close to approximately equal to 1 s [25]. Despite demonstrating a significant improvement of scan rates ($>10\times$) in comparison to the other delay lines that existed that time, the pixel dwell times accomplished by this scheme falls short of what is expected for microscopy. Over the years, an acousto-optic programmable dispersive filter (AOPDF) has established itself as a trusted fast delay line serving exactly this purpose [36–38]. Using the AOPDF as a fast delay line, we demonstrated in our previous work, low-frequency hyperspectral Raman imaging with a pixel dwell time of 25 μs using a shot-noise limited detection apparatus [39].

In addition to impulsively exciting a Raman active medium and extracting the (pump) bandwidth-limited Raman spectrum using various read-out mechanisms, there has also been significant work done in the past in developing coherent control mechanisms where selective excitation of modes has been accomplished using shaped pump pulses. Demonstrated by Nelson *et al.* [40] in the optical generation of tunable ultrasonic waves, where a sequenced pair of pump pulses were used to enhance, cancel, or phase shift the coherently generated acoustic waves, Weiner *et al.* [41,42] extended this idea to optical control of molecular motion by using time-sequenced femtosecond pulses. Coherent control techniques have thrived since then in which appropriately shaped pump pulses have been used to selectively amplify or suppress a desired mode [43–50]. An imaging application using such coherent control mechanisms was demonstrated by Dudovich *et al.* [46]. However, in this work, the use of a spectral filter to isolate the generated coherent anti-Stokes Raman scattered (CARS) photons from the input spectrum limited the lowest accessible vibrational frequency to 400 cm^{-1}.

Analogous to the role of the pump pulse in selective excitation is the role of a probe pulse in selective detection. Several papers have considered spectrally resolved detection using a chirped probe pulse to modulate the Raman spectrum of the detected molecules both in the nonresonant [51–53] and resonant cases [53]. Although these works were limited to a spectroscopic context, they showed the ability of a shaped probe pulse to dramatically alter the recorded molecular spectra (i.e., revealing or masking Raman lines). In here we adopt a different detection scheme that is more suited for molecular imaging where the probe-pulse spectrum is integrated and detected with a fast single pixel detector (photodiode). We explore the temporal shaping of the probe pulse to perform selective vibrational detection and imaging. The AOPDF, which is an ultrafast delay line and a pulse shaper, enables us to exemplify two distinct pulse-shaping strategies—the first strategy involves a pair of probe pulses and the second strategy uses a chirped-probe pulse. We demonstrate numerically and experimentally that the two-pulse probe technique functions as a tunable vibrational notch filter while the chirped-probe technique functions as a vibrational low-pass filter.

Figure 1(a) shows a schematic of the experimental setup used in this work. A Chameleon OPO-VIS (Coherent), which consists of a titanium sapphire (TiSa) laser produces a 80-MHz pulse train at 800 nm, which is used to pump an optical parametric oscillator (APE, fs OPO)—the signal output of which is tuned to 1040 nm. The 1040 nm and the 800 nm beams function as the pump and the probe beams, respectively. The pump pulse has a bandwidth of 9.1 ± 0.3 nm while the probe pulse has a bandwidth of 5.45 ± 0.2 nm. It is to be noted that the wavelengths of the pump and probe beams are far from the electronic resonances for the samples considered in this study. The pump beam is modulated at 12 MHz using an acousto-optic modulator (AOM) (MT200-A0.2-1064, AA Opto-Electronic, France), which is externally driven by a function generator (AFG1062, Tektronix, France). The pump beam then goes through a double-pass custom transmission grating pair (Wasatch Photonics, USA), with 600 lines per millimeter to compensate for the positive dispersion accumulated with propagation through the optical components in the system such that it has a transform-limited pulsewidth of approximately equal to 175 fs at the sample plane. The pulse shaping of the probe beam in order to create the two-pulse structure and the chirped-probe structure is done using the AOPDF (Dazzler WB, Fastlite).

The two-pulse probe structure is achieved by loading two acoustic waves in the Dazzler, the separation of which allows us to tune the intrapulse distance (T). Indeed, as the diffraction efficiency of the AOPDF is less than one, one optical pulse that encounters two acoustic waves inside of the crystal will be diffracted twice at different delays, thus creating a pair of pulses. Such a scheme can be used for

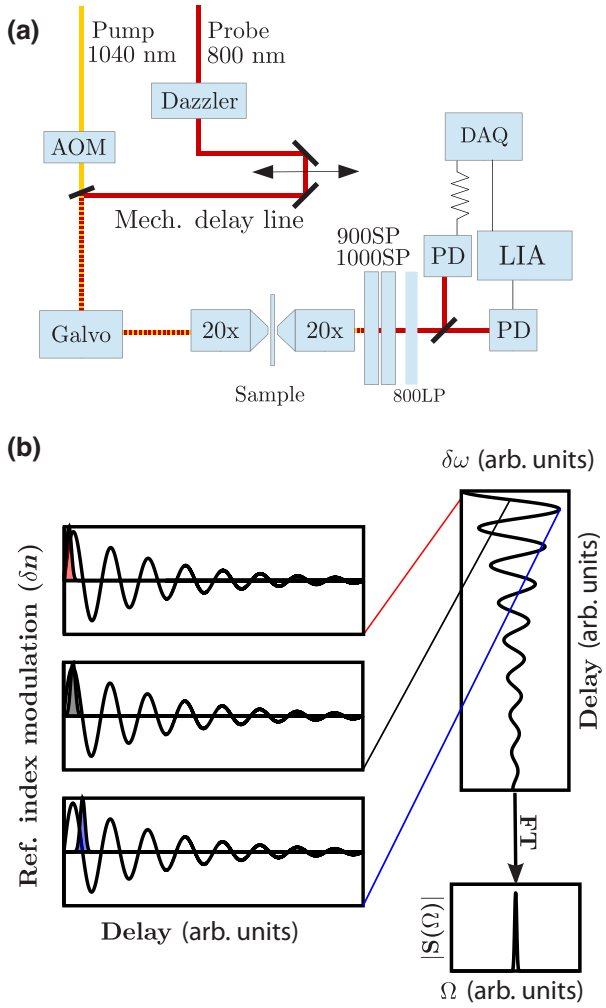

FIG. 1. (a) The figure pictorially represents the key components of the setup. PD, photodiode; Galvo, galvanometric mirrors; AOM, acousto-optic modulator; DAQ, data acquisition card; LIA, lock-in amplifier; SP, short pass; LP, long pass. (b) The figure pictorially represents the logic of the spectral shift detection. The damped sinusoid represents the index variation in time due to the Raman oscillations. The Gaussian function represents the probe-pulse field spectrum. Depending on the arrival time of the probe pulse with respect to the pump pulse, it sees a rising or falling edge of the refractive index, which translates to a red or blue shift in the spectral centroid of the pulse [17] (indicated here by the color of the pulse). Allowing the probe pulse to pass through an edge filter centered at the probe central frequency, this spectral shift is converted to an intensity modulation in time, the Fourier transform of which gives the vibrational spectrum.

self-interferometry [54]. The phases of the two pulses are manipulated through their respective acoustic waves such that both pulses are transform-limited pulses at the sample plane (approximately equal to 170 fs). For the chirped-probe structure, a single acoustic wave is loaded in the Dazzler and the second-order phase is tuned to imprint different chirp values, allowing us to control the chirp of the pulse at the sample plane.

The probe beam then travels through a mechanical delay line (M 415.2S, Physik Instrumente, Germany) in order to catch up with the extra optical path length the pump beam travels in the OPO cavity. Another role of the mechanical delay line is to globally shift the scanning window of the Dazzler, which allows us to stitch data from multiple scan windows of the Dazzler for measuring longer delays. The pump and probe beams are recombined by using a dichroic mirror and fine-tuned for collinearity. The recombined beams are then sent into a inverted microscope (Eclipse Ti-U, Nikon, Japan) equipped with galvanometric scan mirrors (6215HM60, Cambridge Technology). The scan mirrors are conjugated to the back focal plane of the microscope objective using a 2× telescope. The beams are focused and collected with 20x/0.75NA air objectives (CFI Plan Apo Lambda 20X, Nikon).

The collected light is then sent to our detection unit. The pump beam is blocked by using a set of optical filters (2 × FES0900, Thorlabs, USA and 2 × FES1000, Thorlabs, USA). An edge filter (FELH800, Thorlabs, USA) centered at the probe central frequency is used to convert the frequency shift into an intensity modulation at the photodiode. The back focal plane of the collection objective is conjugated to the active area of two photodiodes—one to detect the modulation transfer from the pump to the probe (SRS Lock-in Module, APE, Germany) and the other to detect the integrated transmission of the probe (DET100A, 8-MHz bandwidth). The lock-in amplifier receives its reference input from the same channel of the function generator that drives the AOM.

The output of the lock-in amplifier is connected to a fast waveform digitizer card (ATS460-128M PCI Digitizer, 125 MS/s, AlazarTech, Canada) through a 1.35-MHz low-pass filter (EF508 Thorlabs, 5^{th}order). The different components of the experimental setup are controlled using a custom made Labview interface (Labview2011, National Instruments, USA). A National Instruments input-output card (NI 6361, National Instruments, USA) is used to control the galvanometric mirrors, to trigger the data acquisition on the AlazarTech digitizer and to trigger the Dazzler.

Figure 1(b) illustrates the logic of the frequency-shift detection technique. The damped sinusoid depicts the time-varying refractive index activated due to the impulsive pump excitation. The time derivative of the oscillating refractive index results in a phase modulation and a corresponding centroid shift of the probe's power spectrum, which depends on the phase of the vibration as the probe passes through the sample. An optical edge filter centered at the central frequency of the probe converts this spectral centroid shift to an intensity modulation at the photodiode. This intensity modulation allows one to record directly the

time response of the sample, and a Fourier transform of the acquired signal (at positive delays exceeding the pulses durations) reveals the vibrational frequencies.

Taking note of the logic of the spectral shift detection, here, we develop first a two-pulse probe structure with an intrapulse distance such that one pulse sees a leading edge of the refractive index while the other sees a falling edge [Fig. 2(a)]. Given that the two pulses have an intrapulse separation shorter than the integration time of the photodiode, the photocurrents generated in the photodiode incoherently sum to a total value that is proportional to the total incident power after passing through the edge filter. It is this photodetection property that allows for selective detection of particular vibrational modes in the two-pulse case. At a suitable delay between the probe-pulse pairs, the increase in transmitted power through the detection edge filter of one of the probe pulse from a rising phase modulation is counteracted by a decrease in transmitting power through the edge filter of the second probe pulse. A mode for which the net frequency shift and thereby the net photocurrent is constant at all delay points goes undetected [Fig. 2(c)]. This is analogous to having a vibrational notch filter that blocks a particular mode. To state this mathematically, a mode (neglecting the exponential decay) is suppressed by creating a probe-pulse pair with an intrapulse temporal distance equal to an odd integer multiple of the half-period of the mode.

$$T = \frac{(2n+1)}{2}\tau_m \quad n\epsilon\mathcal{Z}, \tag{1}$$

where τ_m is the period of the mode.

In the chirped-probe detection [Figs. 2(b) and 2(d)] the degree of freedom is the second-order spectral phase (ϕ_2) of the probe pulse, which is linked to the spectral phase (ϕ) as,

$$\phi(\omega) \approx \frac{1}{2}\phi_2(\omega) \times (\omega - \omega_0)^2. \tag{2}$$

It can be shown that the second-order spectral phase results in temporal stretching of a transform-limited pulse [55]. This allows us to build an intuitive time-domain picture for the chirped-probe experiments. A mode gets undetected in the spectral shift technique when the probe pulse duration roughly matches the period of the mode. This is because the probe pulse is too long as compared to the period of the time-varying refractive-index profile to experience a red, or blue shift [see Fig. 2(d)]. This is attributed to the way the input probe field and the scattered fields interfere under such conditions. The modes go undetected in decreasing order of energy and thereby enabling the chirped-probe to function as a tunable vibrational low-pass filter. The mode attenuation happens on top of the preferential detection due to the bandwidth of the probe pulse, as demonstrated in Ref. [17]. The general dependence of the mode attenuation

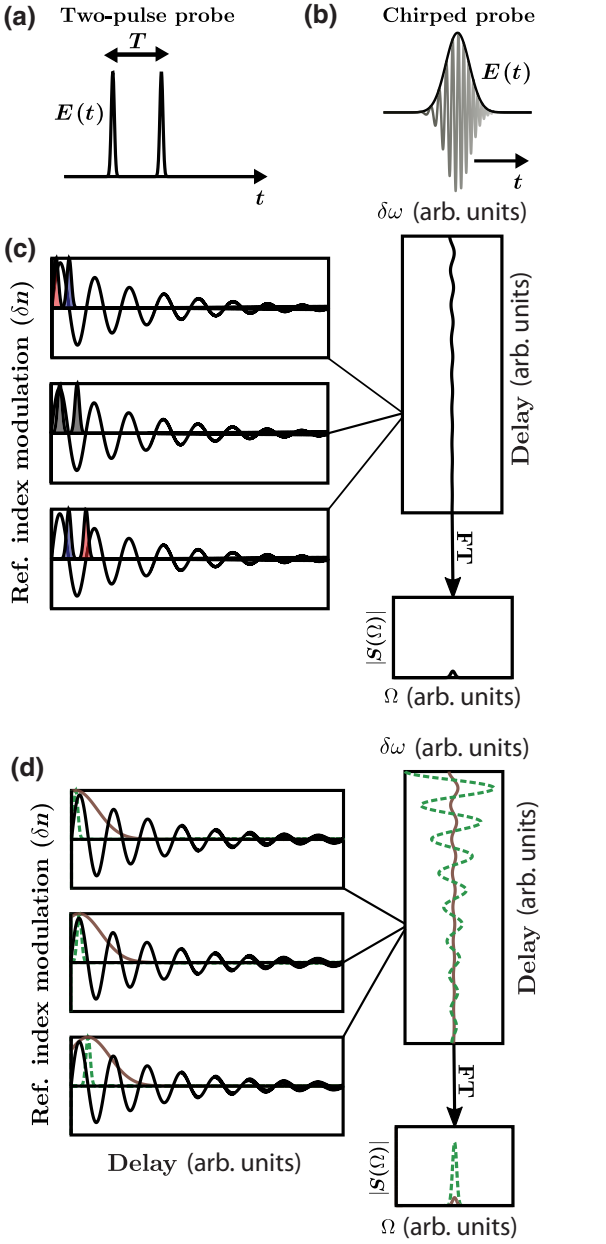

FIG. 2. (a),(b) Pictorial representation of the two-pulse probe structure and the chirped-probe structure arriving with a varying delay after a transform-limited excitation pump pulse has excited the vibrational coherence in the sample. (c) When the intraprobe pulse distance is equal to an odd integer multiple of half the vibrational period, the redshift experienced by one pulse compensates the blue shift experienced by the other pulse (indicated by the color of the pulse), thereby inhibiting the detection of the mode via spectral shift detection. (d) The Gaussian functions represent the probe-field amplitudes of a transform-limited probe pulse (the dashed green) and a chirped pulse (the solid brown). It is seen that with a transform-limited probe pulse, whose period is shorter than the period of the mode, the spectrum of the mode is well retrieved. As the pulse is chirped, the pulse gets broader in time and eventually surpasses the mode period. When this happens the interference between the input and the scattered fields evolve in such a way that the spectral centroid shift goes down and makes the Raman line disappear in the spectrum.

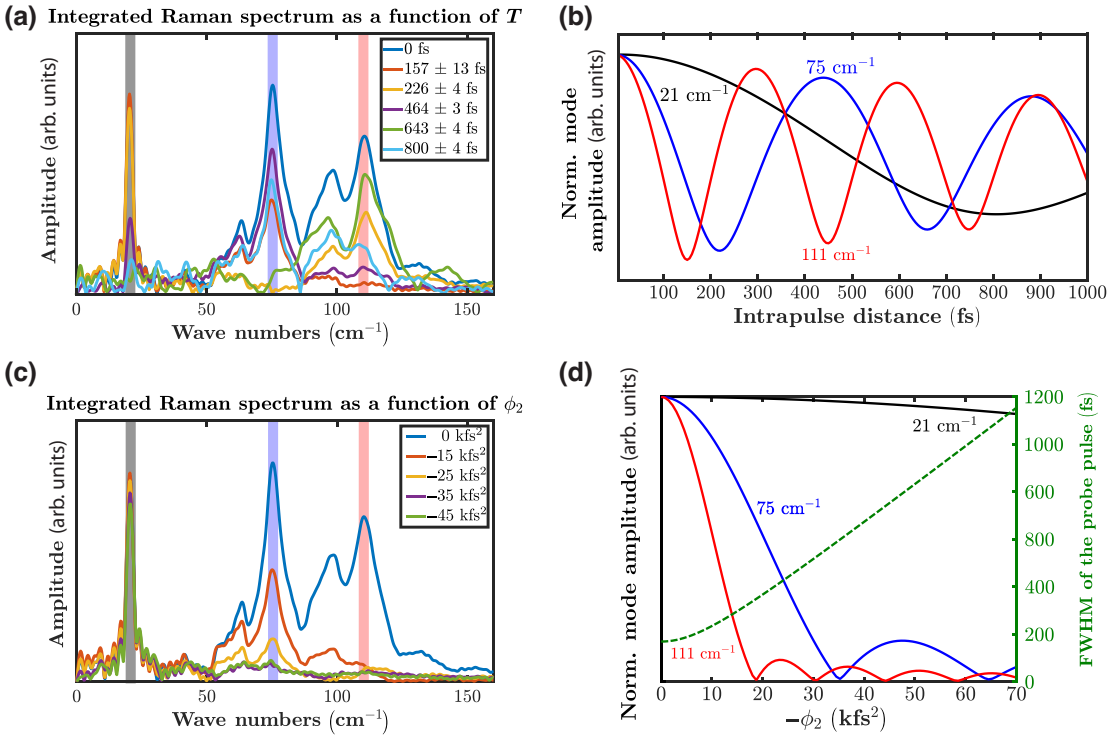

FIG. 3. (a),(c) Experimentally acquired spectra of CBZDH using the two-pulse probe structure and the chirped-probe structure, respectively. In the two-pulse probe scheme (a) a spectral line disappears when intrapulse temporal distance T is equal to an odd integer multiple of the half-period of the vibration mode. In the chirped-probe scheme (c) the higher wave-number modes disappear when the probe pulse chirp is increased. The experimental results are in good agreement with the numerical estimation of the mode amplitudes using these two techniques (b),(d). For instance comparing (a),(b) it can be seen how the 111 cm^{-1} mode goes undetected at $T \approx 157$ fs, which is close to the half-period of this mode (which is 150 fs). Similarly, comparing (c),(d) it is seen that the 111 cm^{-1} mode is undetected at approximately equal to -15 kfs^2, which broadens the pulse to approximately equal to 300 fs, which is the period of this mode.

on the probe-pulse duration and probe bandwidth is numerically demonstrated for the 75 cm^{-1} mode of CBZDH in the Appendix. All the results presented in this work are under the consideration that the probe-pulse bandwidth is large enough for a mode to be sensitive to spectral-shift detection, such that it can be later played around with by varying the chirp on the probe pulse.

To acquire Raman spectra and images, we stitch data from five successive Dazzler scan windows (each of the Dazzler windows being 3.5 ps). Given that all the measurements in this section correspond to one accumulation (i.e., without any averaging), the total image-acquisition time over a field of view of 300 μm (2500 pixels with a pixel dwell time of 25 μs) is 0.312 s. We do not show here the time traces recorded in each measurement since the suppression and revival of a mode is more striking in its spectrum. For the measurements reported in this paper, the pump and the probe beams had an average power of 60 mW at the sample plane. Figures 3(a) and 3(c) show the experimental image integrated spectra of carbamazepine dihydrate (CBZDH) as a function of the intrapulse distance (T) and the second-order phase values (ϕ_2). For instance, the red stripes in these figures show how the 111 cm^{-1} mode is selectively detected by these two techniques. In Fig. 3(a), the spectral line at 111 cm^{-1} disappears at T values 157 and 464 fs, which are odd integer multiples of the half-period of the mode (approximately equal to 150 fs). In Fig. 3(c), it is seen that the 111 cm^{-1} mode is undetected at $\phi_2 \approx -15$ kfs^2, which broadens the pulse to approximately equal to 300 fs, which is the period of this mode. The results from the modeling in MATLAB [Fig. 3(b) and 3(d)] predicting the evolution of the mode amplitudes are in good agreement with the corresponding experimental data. The details about the modeling can be found in the Supplemental Material. It is to be noted that in Fig. 3(b) the normalized amplitude of each mode goes from 1 to 0, however, with different modulation depths since the mode amplitude recorded via spectral-shift technique is a function of the probe-pulse bandwidth. Here the plots have been overlapped to compare how the modes evolve as a function of the intrapulse distances rather than to compare the extinction of one with respect to the other.

The hyperspectral images (pixel dwell time of 25 μs) are shown in Fig. 4(b) with Fig. 4(a) being the optically

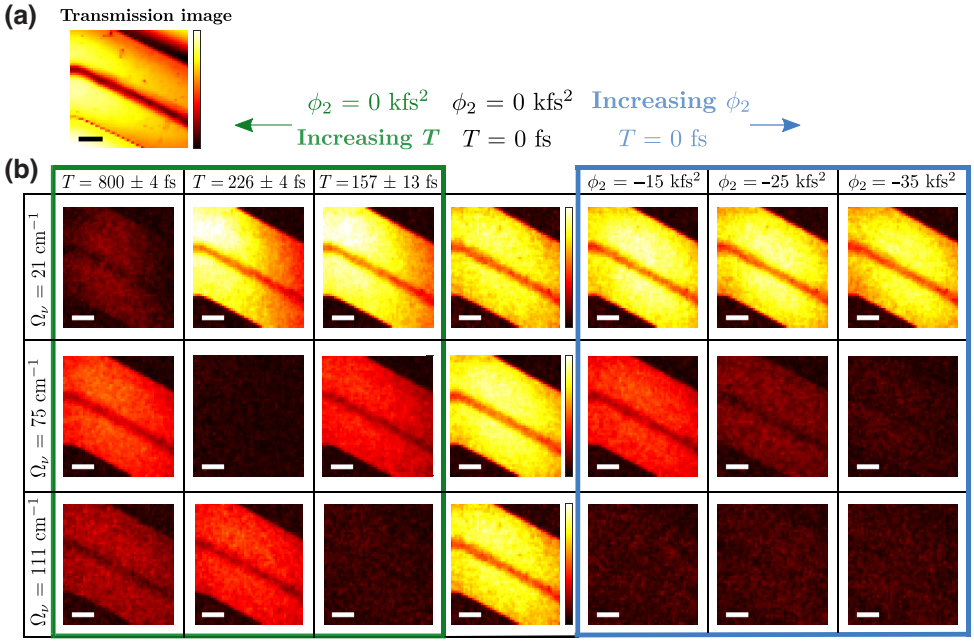

FIG. 4. Hyperspectral images of CBZDH using the two-pulse probe and the chirped-probe structures. (a) The optically resolved transmission image of the crystal. (b) Table of figures showing how the hyperspectral images evolve with the two detection modalities. The movie of the hyperspectral images as a function of T and ϕ_2 emphasizes the fact that two-pulse structure functions as a tunable vibrational notch filter while the chirped-probe functions as a tunable vibrational low-pass filter. The signal in each pixel corresponds to a spectral integration over 0.75 cm^{-1} around the peak. Scale bar: 60 μm. Image pixel dwell time: 25 μs.

contrasted transmission image of the crystal. The signal in each pixel corresponds to a spectral integration over 0.75 cm^{-1} around the peak. All the hyperspectral images in this section are smoothened with a Gaussian filter of standard deviation of 0.55. Further, the signal in each channel (each mode), for a certain T or ϕ_2 value, is normalized with the signal of the same channel corresponding to $T = 0$ fs and $\phi_2 = 0$ kfs^2. Stated in other words, this implies that the scale bar of a particular channel has nothing to do with the scale bar of another channel, however, for a given channel, the scale bar of the image corresponding to $T = 0$ fs and $\phi_2 = 0$ kfs^2 is applied to the rest of the images (corresponding to different T and ϕ_2 values, respectively). The table of figures emphasizes the fact that two-pulse structure functions as a tunable vibrational notch filter while the chirped-probe functions as a tunable vibrational low-pass filter. The figures at the central column correspond to the measurement made using a transform-limited probe pulse. To the right, we see how increasing the chirp attenuates the signal from various channels in decreasing order of energy (vibrational low-pass filter). To the left, we see how increasing the intrapulse distance of a two-pulse probe structure selectively notches (vibrational notch filter) the signal from the desired channel.

To further showcase this effect, Fig. 5 shows a two-pulse probe measurement made with a composite sample (CBZDH+anthracene) in one field of view. Figure 5(a) shows the optically resolved transmission image of the crystals with the anthracene crystal on the left and the CBZDH crystal on the right. Figure 5(b) shows the numerical prediction of the evolution of the 40-cm^{-1} mode of anthracene and the 75-cm^{-1} mode of CBZDH as a function of the intrapulse distance. The power of the two-pulse probe technique is evident from the way the two chemical species are uniquely contrasted [Fig. 5(c)] just by tuning the intrapulse distance.

To conclude, using an AOPDF to shape and delay the probe pulses in time, we perform vibrational selective detection and fast imaging (pixel dwell time of 25 μs) in the low-frequency regime. This work investigates the lines of shaping the probe pulse for this purpose in contrast to the numerous works reported so far, which involve the shaping of the pump pulse. We numerically model and experimentally verify two pulse-shaping strategies—(1) a two-pulse probe structure that functions as a tunable vibrational notch filter and (2) a chirped-probe structure that acts as a tunable vibrational low-pass filter. The two-pulse structure finds immediate application when one wishes to detect a small peak that is overlapped by a stronger peak in the molecular spectrum. By tuning the intrapulse distance, the two-pulse structure can be used to selectively suppress the strong peak from the detected spectra, thereby enhancing the visibility of the weaker peak. On the other hand, if the spectral amplitude of an energetically lower peak

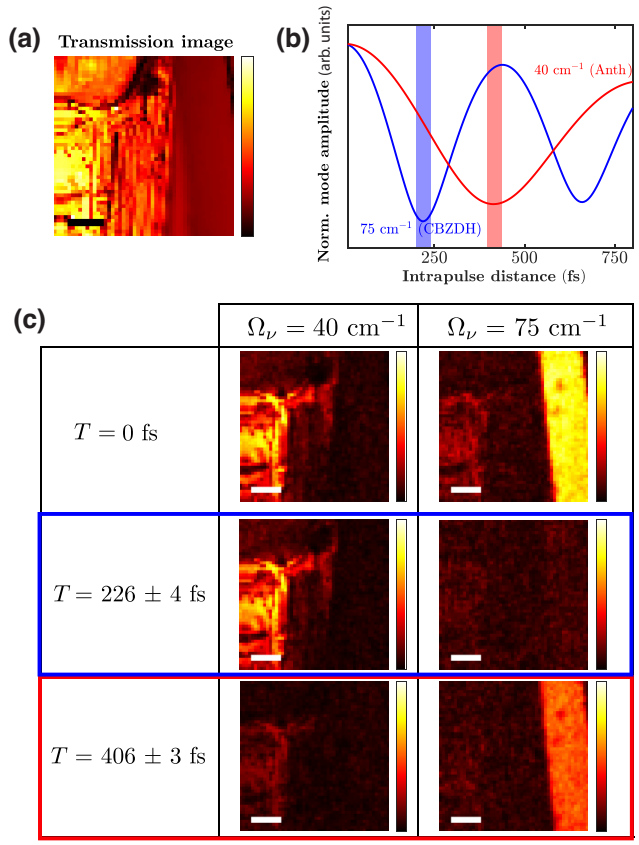

FIG. 5. Hyperspectral images of a compound sample of CBZDH and anthracene using the two-pulse probe. (a) The optically resolved transmission image of anthracene (on the left) and CBZDH (on the right). (b) Numerical result showing the trend of the 40 cm^{-1} mode of anthracene and the 75 cm^{-1} mode of CBZDH as a function of the intrapulse distance. (c) The hyperspectral images of the crystals at the intrapulse distances highlighted in (b). The signal in each pixel corresponds to a spectral integration over 0.75 cm^{-1} around the peak. The image nicely exhibits selectively imaging a particular chemical species by simply tuning the T value of the two-pulse structure. Scale bar: 60 μm. Image pixel dwell time: 25 μs.

is much smaller than that of energetically higher peaks, which eventually occupy most of the detector dynamic range, then the second strategy proves to be valuable in improving the visibility of the weaker peak by becoming insensitive to the higher-frequency components by a simple variation of the second-order phase of the probe pulse. Stated loosely, both techniques aid in synthetically enhancing the dynamic range of detection at the frequency of interest, although the notch filter is expected to be more relevant for the applications.

We acknowledge financial support from the Centre National de la Recherche Scientifique (CNRS), Weizmann Institute of Sciences, ANR grants (ANR-11-IDEX-0001-02, ANR-10-INSB-04-01, ANR-11-INSB-0006, ANR-16-CONV-0001, ANR-21-ESRS-0002 IDEC), INSERM PC201508, 18CP128-00, 22CP139-00. This project has received funding from European Union's Horizon 2020 EU ICT 101016923 CRIMSON and European Research Council (ERC, SpeckleCARS, 101052911). Views and opinions expressed are, however, those of the author(s) only and do not necessarily reflect those of the European Union or the European Research Council. Neither the European Union nor the granting authority can be held responsible for them.

APPENDIX A: LOGIC OF THE NUMERICAL MODEL

The numerical modeling of the experiments was done in MATLAB. We start by defining the probe field. For simplicity, we ignore the vectorial nature of the field and treat it as a scalar function. Further, we suppress the spatial dependence of the field but its temporal dependence is assumed. The real probe electric field $E_{\rm pr}(t)$ can be written as the real part of an analytic function $\underline{E}_{\rm pr}(t)$:

$$E_{\rm pr}(t) = {\rm Re}\{\underline{E}_{\rm pr}(t)\},$$

where $\underline{E}_{\rm pr}(t)$ in the slow varying envelope approximation (SVEA) reads

$$\underline{E}_{\rm pr}(t) = \underline{A}_{\rm pr}(t)\exp(i\omega_0 t),$$

where ω_0 is the central frequency and $\underline{A}_{\rm pr}(t)$ is the total complex temporal pulse envelope. We use $\underline{A}_{\rm pr}(t)$ to define our pulse in the model.

The next step is to account for the Raman phase modulation. The pump pulse activates the vibrational coherence, which is probed by the probe pulse at a relative delay τ. The phase modulation due to the Raman oscillations reads

$$\delta\phi_R(t) = \sum_{v,mn} \delta\phi_R^{v,mn}(t) = \sum_{v,mn} \delta\phi_0^{v,mn} h_v^{mn}(t)$$

where v accounts for different modes and m, n account for vibrational energy levels. $\delta\phi_0^{v,mn}$ is the peak phase shift. $h_v^{mn}(t)$ is the impulse response function, which reads

$$h_v^{mn}(t) = H(t)e^{-(1/2)\Gamma_{v,mn}t}\sin(\Omega_{v,mn}t),$$

where $H(t)$ is the heaviside step function, $\Gamma_{v,mn}$ is the dephasing rate and $\Omega_{v,mn}$ is the vibrational beat frequency. In our model, without loss of generality, all the modes are equally weighed and assumed to have the same linewidth ($\Gamma_{v,mn} = 6$ cm^{-1}). For carbamazepine dihydrate, these parameters would then be, $\delta\phi_0^{v,mn} = 1$, $\Omega_{v,mn} = 21, 75$, and 111 cm^{-1} and $\Gamma_{v,mn} = 6$ cm^{-1}.

The schematic (Fig. 6) represents the logic of the model. We start in the time domain, where, for each pump-probe delay τ, the probe field, $\underline{A}_{\rm pr}(t;\tau)$, senses the phase modulation due to the Raman oscillations, $\delta\phi_R(t)$. We then pass

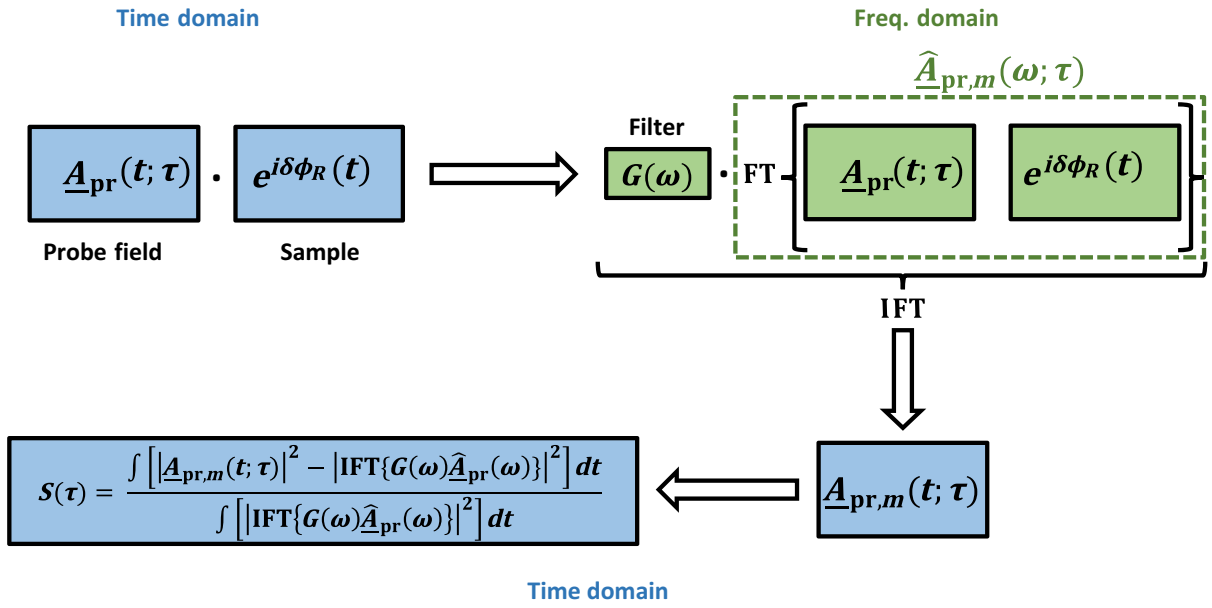

FIG. 6. Logic of the model: the schematic captures the general logic of the model. We start in the time domain by finding the product between the field $\underline{A}_{\mathrm{pr}}(t;\tau)$ and the phase modulation due to the Raman oscillations, $\delta\phi_R(t)$. To estimate the impact of the temporal phase modulation on the probe's spectrum, we pass on to the frequency domain where we perform spectral filtering through the filter function $G(\omega)$. Taking into account the effect of the spectral filter, we go back to the time domain where we compute the differential signal $S(\tau)$ through the modulated field $\underline{A}_{\mathrm{pr},m}(t;\tau)$ and the unmodulated field.

to the frequency domain where the effect of the optical edge filter is contained in the definition of the filter function, $G(\omega)$. Once the filter effect is accounted for, we do an inverse Fourier transform and obtain the time-domain probe field, $\underline{A}_{\mathrm{pr},m}(t;\tau)$, which has in it now the information about the phase modulation and spectral filtering. Finally, we compute the differential signal, $S(\tau)$, which gives the temporal Raman response that we record in an actual experiment.

For the two-pulse probe experiment, we define the probe field as the sum of two Gaussian pulses with an intrapulse distance (T):

$$\underline{A}_{\mathrm{pr}}(t;\tau;T)=e^{-\left((t-\tau)^2/2\tau_p^2\right)}+e^{-\left((t-\tau-T)^2/2\tau_p^2\right)},$$

where τ_p is linked to the temporal FWHM of the pulse (intensity) as $\tau_{0,\mathrm{FWHM}}=2\sqrt{\ln 2}\tau_p$. And for the chirped probe, we define the probe field as

$$\underline{A}_{\mathrm{pr}}(t;\tau;\phi_2)=\frac{1}{\sqrt{1+i(\phi_2\tau_p^{-2})}}e^{-(1/2)[(t-\tau)^2/(\tau_p^2+i\phi_2)]},$$

where ϕ_2 is the second-order spectral phase.

In the case of the two pulse-probe (chirped probe) experiment, we run *for* loops over different intrapulse distance (second-order phase) values and compute the differential transmission through the spectral filter, as a function of the pump-probe delay parameter (τ). A Fourier transform of the delay scan over τ gives us the vibrational spectrum.

APPENDIX B: MODE AMPLITUDE EVOLUTION AS A FUNCTION OF TRANSFORM-LIMITED PULSE WIDTH AND CHIRP VALUE

The transform-limited (TL) pulse duration of the probe pulse, or in other words its bandwidth, determines the extent of the spectral overlap between the incident field and the scattered fields (by the molecular vibration modes). As highlighted in our work, a chirped probe function acts as a vibrational low-pass filter, however, the caveat is that the transform-limited pulse (i.e., when $\phi_2=0$) must have a bandwidth that allows for effective interference with the scattered field (that appears as spectral side bands). In the time-domain picture, the probe pulse must be short enough to resolve the refractive-index transient resulting from the molecular vibration modes (i.e., shorter than the mode period).

This is evident from Fig. 7 where the mode amplitude evolution of the 75-cm^{-1} mode of CBZDH is shown as a function of the transform-limited probe-pulse duration and its second-order phase value. It is seen that as the TL pulse temporal width of the probe pulse increases, the chirp value required to attenuate the detected mode amplitude decreases. Eventually, when the probe-pulse duration is comparable to the mode duration (444 fs), the sideband

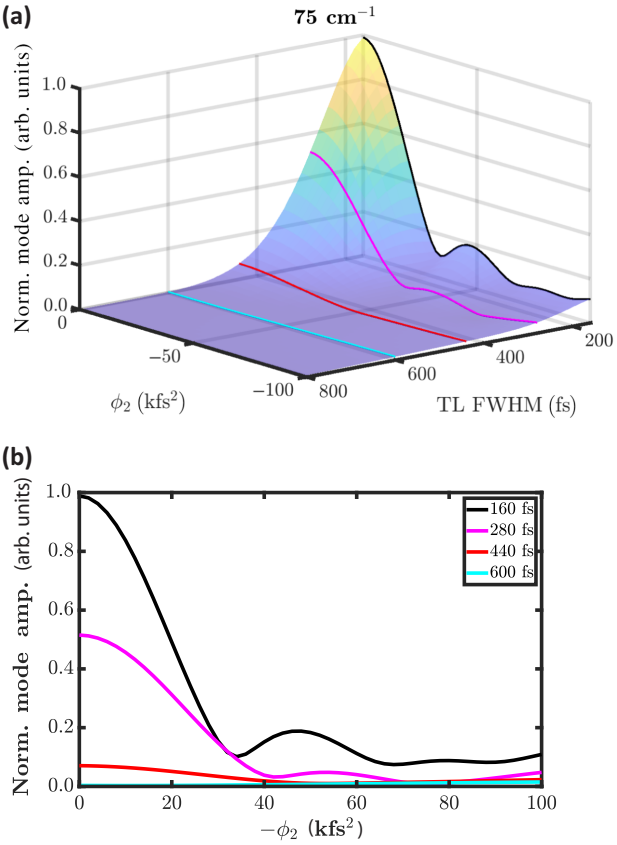

FIG. 7. Mode amplitude evolution as a function of TL FWHM: (a),(b) depict the dependence of the mode amplitude of the 75 cm^{-1} mode of CBZDH as a function of the TL temporal pulse width (i.e., the FWHM when $\phi_2 = 0$) and the second-order phase (ϕ_2). The black curve corresponds to the TL FWHM relevant to our experiments (approximately equal to 160 fs). As the TL FWHM becomes longer, the sideband interference becomes weaker and hence the chirp required to extinguish the mode from being detected goes down (depicted by the pink and red curves). At long enough pulse durations, there is no overlap between the incident and the scattered fields making the probe pulse insensitive to spectral-shift detection (represented by the cyan curve).

spectral interference is so weak that the signal measured via the spectral-shift technique vanishes.

[1] K. Thorn, A quick guide to light microscopy in cell biology, Mol. Biol. Cell. **27**, 219 (2016).

[2] S. Ruhman, A. Joly, B. Kohler, L. Williams, and K. Nelson, Intramolecular and intermolecular dynamics in molecular liquids through femtosecond time-resolved impulsive stimulated scattering, Rev. Phys. Appl. **22**, 1717 (1987).

[3] B. M. Fischer, M. Walther, and P. U. Jepsen, Far-infrared vibrational modes of DNA components studied by terahertz time-domain spectroscopy, Phys. Med. Biol. **47**, 3807 (2002).

[4] T. R. Globus, D. L. Woolard, T. Khromova, T. W. Crowe, M. Bykhovskaia, B. L. Gelmont, J. Hesler, and A. C. Samuels, THz-spectroscopy of biological molecules, J. Biol. Phys. **29**, 89 (2003).

[5] K. G. Brown, S. C. Erfurth, E. W. Small, and W. L. Peticolas, Conformationally dependent low-frequency motions of proteins by laser Raman spectroscopy, Proc. Natl. Acad. Sci. **69**, 1467 (1972).

[6] R. R. Jones, D. C. Hooper, L. Zhang, D. Wolverson, and V. K. Valev, Raman techniques: Fundamentals and frontiers, Nanoscale Res. Lett. **14**, 1 (2019).

[7] J. Reintjes, M. D. Duncan, and T. J. Manuccia, Scanning coherent anti-Stokes Raman microscope, Opt. Lett. **7**, 350 (1982).

[8] A. Zumbusch, G. R. Holtom, and X. S. Xie, Three-Dimensional Vibrational Imaging by Coherent Anti-Stokes Raman Scattering, Phys. Rev. Lett. **82**, 4142 (1999).

[9] E. Ploetz, S. Laimgruber, S. Berner, W. Zinth, and P. Gilch, Femtosecond stimulated Raman microscopy, Appl. Phys. B **87**, 389 (2007).

[10] J. X. Cheng and X. S. Xie, Vibrational spectroscopic imaging of living systems: An emerging platform for biology and medicine, Science **350**, aaa8870 (2015).

[11] C. L. Evans, E. O. Potma, M. Puoris'haag, D. Côté, C. P. Lin, and X. S. Xie, Chemical imaging of tissue in vivo with video-rate coherent anti-Strokes Raman scattering microscopy, Proc. Natl. Acad. Sci. USA **102**, 16807 (2005).

[12] B. G. Saar, C. W. Freudiger, J. Reichman, C. M. Stanley, G. R. Holtom, and X. S. Xie, Video-rate molecular imaging in vivo with stimulated Raman scattering, Science (New York, N.Y.) **330**, 1368 (2010).

[13] H. Rigneault, N. Forget, and X. Audier, High-speed chemical imaging of dynamic and histological samples with stimulated Raman micro-spectroscopy, Opt. Express **28**, 15505 (2020).

[14] M. Liebel, C. Schnedermann, T. Wende, and P. Kukura, Principles and applications of broadband impulsive vibrational spectroscopy, J. Phys. Chem. A **119**, 9506 (2015).

[15] H. Kuramochi, S. Takeuchi, and T. Tahara, Femtosecond time-resolved impulsive stimulated Raman spectroscopy using sub-7-fs pulses: Apparatus and applications, Rev. Sci. Instrum. **87**, 043107 (2016).

[16] S. De Silvestri, J. G. Fujimoto, E. P. Ippen, E. B. Gamble, L. R. Williams, and K. A. Nelson, Femtosecond time-resolved measurements of optic phonon dephasing by impulsive stimulated Raman scattering in α-perylene crystal from 20 to 300 K, Chem. Phys. Lett. **116**, 146 (1985).

[17] R. A. Bartels, D. Oron, and H. Rigneault, Low frequency coherent Raman spectroscopy, J. Phys.: Photonics **3**, 042004 (2021).

[18] Y. X. Yan, E. B. Gamble, and K. A. Nelson, Impulsive stimulated scattering: General importance in femtosecond laser pulse interactions with matter, and spectroscopic applications, J. Chem. Phys. **83**, 5391 (1985).

[19] D. Raanan, J. Lüttig, Y. Silberberg, and D. Oron, Vibrational spectroscopy via stimulated Raman induced Kerr lensing, APL Photonics **3**, 092501 (2018).

[20] S. Ruhman, A. G. Joly, and K. A. Nelson, Time-resolved observations of coherent molecular vibrational motion and the general occurrence of impulsive stimulated scattering, J. Chem. Phys. **86**, 6563 (1987).

[21] A. Mokhtari and J. Chesnoy, Resonant impulsive stimulated Raman scattering, Europhys. Lett. **5**, 523 (1988).
[22] R. Merlin, Generating coherent THz phonons with light pulses, Solid State Commun. **102**, 207 (1997).
[23] J. K. Wahlstrand, O. E. Martinez, R. Merlin, S. T. Cundiff, and X. Li, Impulsive stimulated Raman scattering: Comparison between phase-sensitive and spectrally filtered techniques, Opt. Lett. **30**, 926 (2005).
[24] T. Ideguchi, S. Holzner, B. Bernhardt, G. Guelachvili, N. Picqué, and T. W. Hänsch, Coherent Raman spectroimaging with laser frequency combs, Nature **502**, 355 (2013).
[25] D. G. Winters, R. A. Bartels, and S. R. Domingue, Time-resolved coherent Raman spectroscopy by high-speed pump-probe delay scanning, Opt. Lett. **39**, 4124 (2014).
[26] D. Oron, D. Raanan, L. Ren, and Y. Silberberg, Impulsive Raman spectroscopy via precision measurement of frequency shift with low energy excitation, Opt. Lett. **43**, 470 (2018).
[27] Y. Soffer, D. Raanan, and D. Oron, Low frequency collinear pre-resonant impulsive stimulated Raman microspectroscopy, ACS Photonics **7**, 3481 (2020).
[28] S. Ruhman, A. Joly, and K. Nelson, Coherent molecular vibrational motion observed in the time domain through impulsive stimulated Raman scattering, IEEE J. Quantum. Electron. **24**, 460 (1988).
[29] E. Gershgoren, H. C. Kapteyn, J. T. Fourkas, M. M. Murnane, R. Tobey, and R. A. Bartels, Simplified setup for high-resolution spectroscopy that uses ultrashort pulses, Opt. Lett. **28**, 361 (2003).
[30] N. A. Smith and S. R. Meech, Optically-heterodyne-detected optical Kerr effect (OHD-OKE): Applications in condensed phase dynamics, Int. Rev. Phys. Chem. **21**, 75 (2010).
[31] J. W. Wilson, P. Schlup, and R. A. Bartels, Synthetic temporal aperture coherent molecular phase spectroscopy, Chem. Phys. Lett. **463**, 300 (2008).
[32] J. W. Wilson, P. Schlup, and R. Bartels, Phase measurement of coherent Raman vibrational spectroscopy with chirped spectral holography, Opt. Lett. **33**, 2116 (2008).
[33] P. Schlup, J. W. Wilson, and R. A. Bartels, Sensitive and selective detection of low-frequency vibrational modes through a phase-shifting Fourier transform spectroscopy, IEEE J. Quantum Electron. **45**, 777 (2009).
[34] K. Hartinger and R. A. Bartels, Modulation of third-harmonic generation conversion in the presence of a rotational wave packet, Opt. Lett. **33**, 1162 (2008).
[35] R. M. Koehl, S. Adachi, and K. A. Nelson, Real-space polariton wave packet imaging, J. Chem. Phys. **110**, 1317 (1999).
[36] O. Schubert, M. Eisele, V. Crozatier, N. Forget, D. Kaplan, and R. Huber, Rapid-scan acousto-optical delay line with 34 kHz scan rate and 15 as precision, Opt. Lett. **38**, 2907 (2013).
[37] I. Znakovskaya, E. Fill, N. Forget, P. Tournois, M. Seidel, O. Pronin, F. Krausz, and A. Apolonski, Dual frequency comb spectroscopy with a single laser, Opt. Lett. **39**, 5471 (2014).
[38] H. Rigneault, N. Balla, and X. Audier, Pump-probe microspectroscopy by means of an ultra-fast acousto-optics delay line, Opt. Lett. **42**, 294 (2017).
[39] D. Oron, D. Raanan, H. Rigneault, M. Asher, M. Menahem, N. Forget, O. Yaffe, S. Shivkumar, and X. Audier, Subsecond hyper-spectral low-frequency vibrational imaging via impulsive Raman excitation, Opt. Lett. **44**, 5153 (2019).
[40] K. A. Nelson, R. J. Miller, D. R. Lutz, and M. D. Fayer, Optical generation of tunable ultrasonic waves, J. Appl. Phys. **53**, 1144 (1982).
[41] A. M. Weiner, D. E. Leaird, G. P. Wiederrecht, and K. A. Nelson, Femtosecond pulse sequences used for optical manipulation of molecular motion, Science **247**, 1317 (1990).
[42] A. M. Weiner, D. E. Leaird, G. P. Wiederrecht, and K. A. Nelson, Femtosecond multiple-pulse impulsive stimulated Raman scattering spectroscopy, JOSA B **8**, 1264 (1991).
[43] L. Dhar, J. A. Rogers, and K. A. Nelson, Time-resolved vibrational spectroscopy in the impulsive limit, Chem. Rev. **94**, 157 (1994).
[44] T. C. Weinacht, R. Bartels, S. Backus, P. H. Bucksbaum, B. Pearson, J. M. Geremia, H. Rabitz, H. C. Kapteyn, and M. M. Murnane, Coherent learning control of vibrational motion in room temperature molecular gases, Chem. Phys. Lett. **344**, 333 (2001).
[45] R. A. Bartels, T. C. Weinacht, S. R. Leone, H. C. Kapteyn, and M. M. Murnane, Nonresonant Control of Multimode Molecular Wave Packets at Room Temperature, Phys. Rev. Lett. **88**, 033001 (2002).
[46] N. Dudovich, D. Oron, and Y. Silberberg, Single-pulse coherently controlled nonlinear Raman spectroscopy and microscopy, Nature **418**, 512 (2002).
[47] D. Oron, N. Dudovich, and Y. Silberberg, Single-Pulse Phase-Contrast Nonlinear Raman Spectroscopy, Phys. Rev. Lett. **89**, 273001 (2002).
[48] D. Oron, N. Dudovich, D. Yelin, and Y. Silberberg, Narrow-Band Coherent Anti-Stokes Raman Signals from Broad-Band Pulses, Phys. Rev. Lett. **88**, 4 (2002).
[49] N. Dudovich, D. Oron, and Y. Silberberg, Single-pulse coherent anti-Stokes Raman spectroscopy in the fingerprint spectral region, J. Chem. Phys. **118**, 9208 (2003).
[50] H. Frostig, O. Katz, A. Natan, and Y. Silberberg, Single-pulse stimulated Raman scattering spectroscopy, Opt. Lett. **36**, 1248 (2011).
[51] I. Gdor, T. Ghosh, O. Lioubashevski, and S. Ruhman, Nonresonant Raman effects on femtosecond pump-probe with chirped white light: Challenges and opportunities, J. Phys. Chem. Lett. **8**, 1920 (2017).
[52] G. Batignani, C. Ferrante, G. Fumero, and T. Scopigno, Broadband impulsive stimulated Raman scattering based on a chirped detection, J. Phys. Chem. Lett. **10**, 7789 (2019).
[53] G. Batignani, C. Sansone, C. Ferrante, G. Fumero, S. Mukamel, and T. Scopigno, Excited-state energy surfaces in molecules revealed by impulsive stimulated Raman excitation profiles, J. Phys. Chem. Lett. **12**, 9239 (2021).
[54] T. Oksenhendler, S. Coudreau, N. Forget, V. Crozatier, S. Grabielle, R. Herzog, O. Gobert, and D. Kaplan, Self-referenced spectral interferometry, Appl. Phys. B **99**, 7 (2010).
[55] J. C. Diels and W. Rudolph, *Ultrashort Laser Pulse Phenomena* (Elsevier, Amsterdam, 2006).